

Observations of stable pickup He^+ tori in a magnetic flux rope at 0.85 au

Chaoran Gu^{1*†}, Lars Berger^{1*†}, Verena Heidrich-Meisner^{1†}, Erik Jentsch¹, Robert F. Wimmer-Schweingruber¹, Lars Seimetz¹

^{1*}Institut für Experimentelle und Angewandte Physik, Christian-Albrechts-Universität zu Kiel, Leibnizstr. 11, 24118, Kiel, Germany.

*Corresponding author(s). E-mail(s): chaorangu@physik.uni-kiel.de; berger@physik.uni-kiel.de;

Contributing authors: heidrich@physik.uni-kiel.de; jentsch@physik.uni-kiel.de; wimmer@physik.uni-kiel.de; seimetz@physik.uni-kiel.de;

[†]These authors contributed equally to this work.

Abstract

Interstellar pickup ions originate from the neutral interstellar medium, are ionized in the heliosphere, and picked up by the solar wind. They initially form a torus-shaped velocity distribution function, which is generally believed to be transformed rapidly into an isotropic shell distribution by pitch-angle scattering. With the SupraThermal Electron Proton onboard Solar Orbiter we observe clear torus-shaped velocity distribution functions at an unprecedented one minute resolution. While these tori are variable on a time scale of one minute, they remain stable for over ten hours without signs of significant scattering. We conclude that they are populated by a huge fraction of the expected total number of pick-up ions injected in the past of the same solar wind stream.

Keywords: Pickup ion, Interstellar medium, Pitch angle scattering

1 Introduction

The heliosphere [1] is surrounded by the local interstellar medium [LISM; 2]. Due to the relative motion of the heliosphere against the LISM, a continuous stream of interstellar neutrals (ISNs) enters the heliosphere with a defined speed and direction. Within the heliosphere, ISNs are subjected to gravitational focusing and ionization processes. The latter depend on location and solar activity through photoionization, electron-impact ionization, and charge exchange [3]. Gravitational focusing leads to a focusing cone [4–7] downwind of the ISN inflow direction, wherein the neutral He densities and consequently the He^+ production rates are higher than outside the focusing cone. Once an ISN is ionized, it is “picked up” by the solar wind plasma and is referred to as an interstellar pickup ion [PUI; 8].

PUIs are a fundamental constituent of the heliosphere and its interaction with the LISM [9, 10]. They also serve as test particles to study fundamental plasma processes. Within a few astronomical units (au) interstellar pickup He^+ is the most abundant interstellar PUI species [11–13].

Interstellar PUIs are continuously injected into the solar wind and can be identified by their low charge states and their characteristic velocity distribution functions (VDFs) [14]. When PUIs are injected, they are subject to the Lorentz force exerted by the convected-by local magnetic field and, thus, spiral around the magnetic field direction. Thereby, their VDF initially forms a torus in velocity space, at a pitch angle (PA) that is defined by the local magnetic field, solar wind conditions, and neutral velocity.

In the dynamic solar wind, such a torus VDF is subjected to multiple processes, such as cooling, heating, PA scattering, or magnetic focusing, that modify its initial shape. Further, depending on their PA PUIs move relative to the solar wind bulk. Most theoretical descriptions of PUI VDFs assume rapid PA scattering to transform the initial torus VDF into an isotropic shell VDF [15–18]. In the expanding solar wind, these shells are expected to be subject to cooling, i.e. collective energy loss. Consequently the continuous injection would result in a filled sphere VDF. For decades observations of PUI VDFs have been studied based on these assumptions [14, 19]. However, there is ample evidence for anisotropies related to the local magnetic field conditions [20–23].

In the past the study of clear anisotropic torus signatures and the time scales of modifying processes have been limited by instrumental capabilities [6, 8, 20–27]. So far, the majority of PUI studies was based on reduced VDFs and averaged over time periods significantly longer than the typical fluctuations in the solar wind conditions. Despite the huge number of studies on He^+ PUIs, we found no He^+ number densities obtained from measurements. Mostly differential phase space densities are reported, or partial densities integrated over the spinning field of view (FOV) of different instruments without any assumption on the PUI VDFs [28].

In this article in Sect. 2, we report on measurements made by the Suprathermal Electron Proton (STEP) instrument of the Energetic Particle Detector [EPD; 29] onboard Solar Orbiter [30] inside a magnetic flux rope observed on November 5, 2021. The results are discussed in Sect. 3 and all details on methods and data are given in Methods 5 after the conclusion in Sect. 4.

2 STEP observations

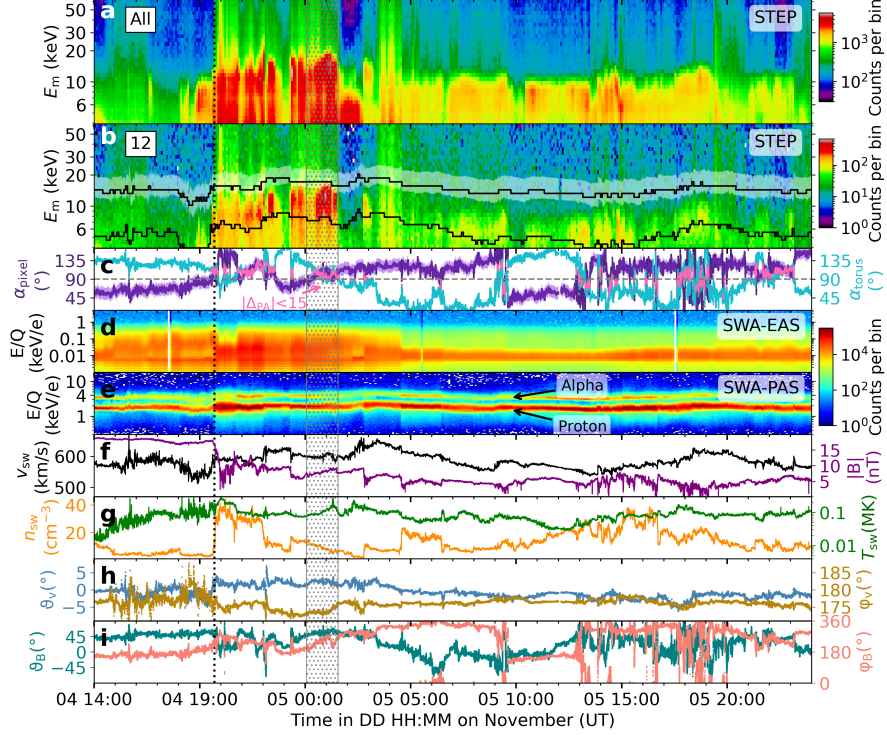


Fig. 1 | Solar Orbiter observations from 2021 November 04, 14:00 UT to 06, 00:00 UT. November 04, 19:42 UT is marked by the dotted line. November 05, 00:04 to 01:34 UT is stippled. **a**, Energy spectrum at 5-minute resolution from STEP/IC, summed from all pixels. **b**, Same as **a** but only pixel 12. The white band is the primary energy range of a shell distribution within this pixel's FOV, and the black lines represent the expected measured energy E_m range of a narrow shell or torus VDF (Methods 5.4). **c**, The PA of the central viewing direction of pixel 12 (α_{pixel}) with $\alpha_{\text{pixel}} \pm 15^\circ$ shaded in light purple, and PA of torus (α_{torus}). Small PA differences ($|\Delta_{\text{PA}}| < 15$) are highlighted in magenta (Methods 5.4). **d**, Summed energy spectrum at 5-minute resolution from EAS1 and EAS2. **e**, Summed Energy spectrum at 5-minute resolution from PAS's whole FOV. **f**, The solar wind speed v_{sw} and magnetic field strength B in the SRF. **g**, Solar wind density n_{sw} and temperature T_{sw} . **h**, v_{sw} elevation angle ϑ_v and azimuthal angle φ_v in SRF. **i**, B elevation angle ϑ_B and azimuthal angle φ_B in SRF.

In this section, we first present an overview of the Solar Orbiter observations of a 34-hour period starts on 2021 November 4, 14:00 universal time (UT). when Solar Orbiter was at a radial distance $R = 0.85$ au, longitude $\lambda = 41.9^\circ$, and latitude $\beta = -2.0^\circ$ in ecliptic coordinates. Then we zoom in on a 90-minute time interval to show detailed STEP observations that show pristine PUI torus distributions in Sect. 2.1. Three one-minute intervals are further analyzed to estimate the He^+ PUI torus injection time scales, injection path lengths, and number densities in Sect. 2.2.

Figure 1 provides an overview of the time period of 2021 November 4, 14:00 UT to November 6, 00:00 UT. It is highly structured and part of a complex interplanetary coronal mass ejection (ICME) event which started earlier with a shock on November 3 at 14:04 UT [31, 32]. The sudden change in magnetic field strength and proton density on November 4 at 19:42 UT (panels f and g, dashed lines) marks the end of a listed ICME [31]. This event is followed by a compression region which likely corresponds to the interface between the first and a following second ICME-like structure [33] that is not previously identified. However, the magnetic field showed a slow rotation for several hours after the interface (panel i), which is a typical signature of a magnetic flux rope.

Embedded in this magnetic flux rope, starting right at the interface on November 4 at 19:42 UT to 01:34 UT the next day, the FOV-integrated STEP observations (panel a) display a clear plateau-like enhancement of suprathermal particles (panel a) up to 20 keV. In the data of STEP pixel 12 (panel b) the enhancement is also visible. But in contrast to the FOV-integrated data, clear pronounced peaks are visible. These peaks are located within the two solid black lines that indicate the expected energy range of a PUI torus or shell signature derived from the local magnetic field and solar wind data (Methods 5.4). Towards higher energies the peaks have a sharp cut-off and are smeared out towards lower energies. Panel c shows the PA of the central viewing direction of pixel 12 α_{pixel} , and of the torus PA α_{torus} expected under local plasma conditions (Methods 5.4). On this pixel, the coincidence of small differences between the two PAs and the observed signatures in panel b fit the expectations for locally injected PUIs that form a torus VDF remarkably well.

In panel d, the Electron Analyser System of the Solar Wind Analyser [SWA-EAS; 34] sees an enhancement of electrons up to a few hundred eV. In EAS data from a year centered on November, 2021, such an enhancement is unusual and the count rates in this energy range are in the highest decile for similar solar wind speeds. In the Proton-Alpha Sensor of the Solar Wind Analyser [SWA-PAS; 34] energy spectra, solar wind protons and alpha particles show clear tracks (panel e). Although PAS measures He^+ over a wider FOV that includes STEP's FOV and up to the velocities expected for PUIs, no clear signatures of He^+ are observed by PAS. Considering the small expected PUI production count rate in PAS (Methods 5.5) this is not surprising since PAS was designed to measure the solar wind bulk and not minor ions. Magnetic field fluctuations and signatures of wave activity that are ubiquitous in the solar wind are on typical levels in our time period of interest after the dashed line (although not shown here).

To differentiate between a torus and a shell VDF in STEP, angular resolution is needed. Therefore, in the following, we investigate individual data of all 15 pixels of STEP. The time variability in both panels a and b, and the differences between the two panels demand a higher temporal resolution than the 5 minutes shown here. Therefore, we selected a 90-minute interval (stippled) that includes a larger substructure within this magnetic flux rope where the enhanced signals in STEP are pronounced for further analysis, and consider all STEP pixels individually.

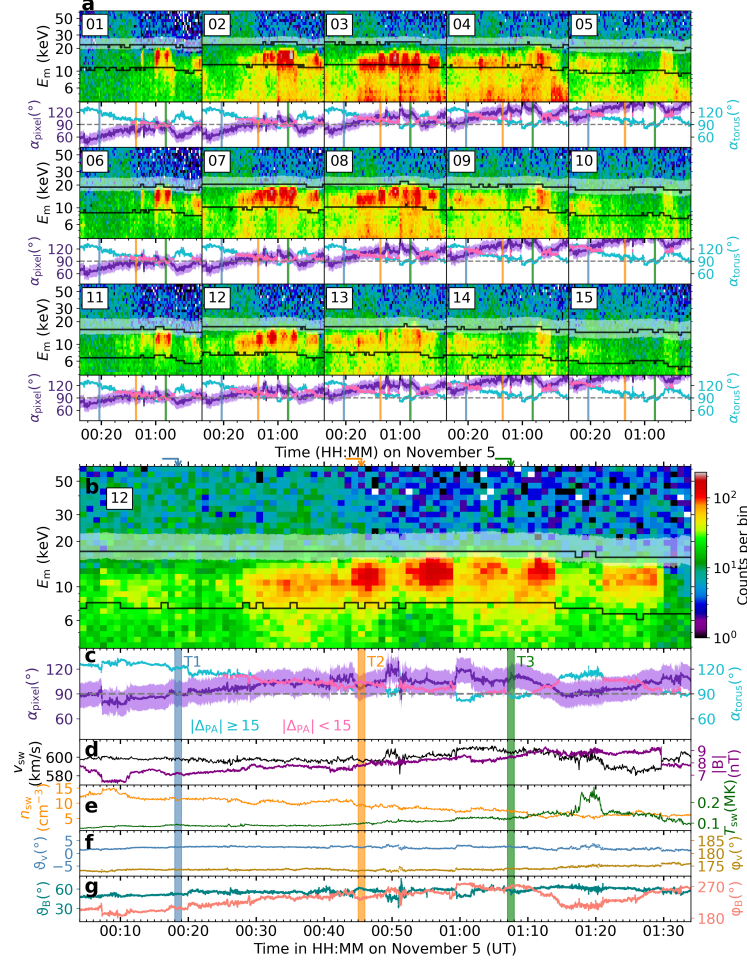


Fig. 2 |Solar Orbiter observations from 2021 November 05, 00:04 to 01:34 UT. **a**, One-minute-integrated energy spectra acquired in the 15 STEP/IC pixels.. The white band and black lines represent the primary energy and measured energy E_m ranges for He^+ with a shell or torus VDF (Methods 5.4). The central viewing direction PA (α_{pixel}) and $\alpha_{\text{pixel}} \pm 15^\circ$, and torus PA (α_{torus}) are given in the panels below. **b-c**, A zoom-in of pixel 12 from **a**. Three color-shaded minutes start at 00:18 (T1), 00:45 (T2), and 01:07 UT (T3) are selected for further investigations. **d-e**, Solar wind conditions in SRF. **f-g**, Elevation angles ϑ_v , ϑ_B and azimuthal angles φ_v , φ_B of \mathbf{v}_{sw} and \mathbf{B} in SRF.

2.1 Signatures of torus VDFs

Figure 2 shows a zoom-in of the stippled time period from Fig. 1. Figure 2d-g reproduce the same parameters as Fig. 1f-i. During this period, the solar wind speed (panel d) was high and stable within 580 km/s to 612 km/s, the solar wind density (panel e) was decreasing gradually and over most of the 90 minutes the magnetic field strength overall gradually increased until a sharp discontinuity at the end (panel d). The magnetic field direction (panel g) was changing smoothly, with a few rapid variations, but generally pointing upwards in the Spacecraft Reference Frame (SRF).

Figure 2a shows the dynamic energy spectra of this time period at one-minute resolution recorded by each of the 15 pixels, along with the pixel and torus PAs (α_{pixel} and α_{torus} , see Methods 5.4). The PA of locally produced PUI torus VDFs is inside the FOV of at least one of STEP’s pixels in the whole period. The peaks observed on pixel 12 in 5 minute resolution in Fig. 1, appear in Fig. 2 on several pixels but not on all pixels in each minute. Overall the peak signatures coincide with small differences $|\alpha_{\text{pixel}} - \alpha_{\text{torus}}| \leq 15^\circ$. The time resolution of 1 minute reveals that these signatures change on this time scale. On the individual pixels the peaks are observed within the expected energy range for a PUI torus or shell VDF. The shape of the signatures is similar to the example of pixel 12 discussed in the context of Fig. 1, i.e. a sharp cut-off towards higher energies and a smearing out towards lower energies is observed. As described in Methods 5.3, pixels 2, 3, and 4 are visibly affected by instrumental aging.

In summary, the observed signatures on all 15 pixels have the following characteristic: they do not appear on all pixels at the same time but coincide with small PA differences on the individual pixels, and they display peaks within the energy range of locally produced He^+ PUI torus or shell VDFs. Thus, we can already conclude that the observed signatures can be clearly attributed to He^+ PUIs, forming torus VDFs that have not been scattered into a shell distribution yet. A detailed discussion follows in Sect. 3. Although the signatures are pronounced with counts exceeding 100 in some energy channels, STEP’s principle of operation (Methods 5.2) does not allow to distinguish between different particle species without further assumptions. Therefore, we investigate three selected minutes in further detail in the next section.

2.2 Properties of observed PUI torus VDFs

To further investigate the relation of expected torus position and torus signatures observed on STEP’s pixels shown in Fig. 2 and to quantify the torus signatures we selected three minutes, T1 (00:18 – 00:19 UT), T2 (00:45 – 00:46 UT), and T3 (01:07 – 01:08 UT), respectively (blue-, orange-, and green-shaded). As described in Methods 5.4, a torus that forms under local conditions can be calculated based on the in situ \mathbf{v}_{sw} , \mathbf{B} , and \mathbf{v}_{inj} .

In Fig. 3a expected torus positions in STEP’s FOV are shown together with the angular coverage of the individual pixels. Therein, the expected torus positions are based on \mathbf{B} in 8 Hz resolution to emphasize their variability. In each of the three minutes these tori are expected to be well within STEP’s FOV, but to be observed on different pixels. Due to the upwards pointing \mathbf{B} the overall situation is similar to an example (Torus 1) discussed in Methods 5.4. In turn, the shape of the observed energy spectra, shown in Fig. 3b in the respective colors, is also similar to that example. In the observations the PUI torus signatures are superposed on signals of other suprathermal particles (Methods 5.6), but clear peaks with a sharp cutoff as expected for torus VDFs can be seen. These peaks (marked by filled circles) appear predominantly on the pixels where they are expected (marked by an \times symbol). All pixels where clear and most pixels where unclear peaks (half-filled circles) are observed but not expected are adjacent to the pixels with the expected torus positions.

For T1 and T3, the expected torus positions and respective observed torus signatures are located at the edges of STEP’s FOV, thus no estimate of the angular width of

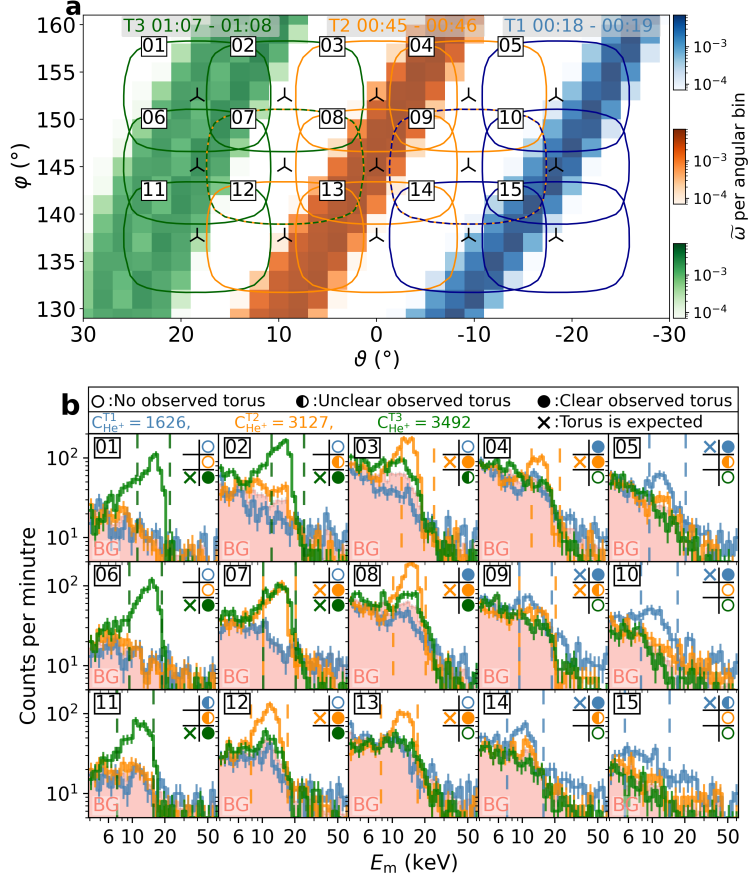


Fig. 3 |Torus positions and energy spectra for three selected minutes. **a**, The expected torus positions based on variations in the 8 Hz magnetic field data are plotted over STEP’s FOV in SRF with elevation angle ϑ and azimuthal angle φ . For each minute and each bin the contained averaged fraction $\tilde{\omega}$ of the expected torus is shown. Boundaries represent 5% of the pixel’s maximum angular response, the color(s) assigned to these boundaries denote the specific torus (or tori) expected on the respective pixel (Methods 5.4). λ symbols indicate central viewing directions. For each minute (marked on top), $\tilde{\omega}$ within each $2^\circ \times 2^\circ$ angular bin is color coded. **b**, The energy spectra for the three selected minutes (color-matched to **a**) together with the estimated background spectra (BG, in pink). The dashed lines mark the respective E_m range, expected for He^+ with a shell or torus VDF. Background-subtracted PUI counts for T1, T2, and T3 are given at the top of panel **b**. Crosses appear when the torus signature is expected by a pixel (Methods 5.4), three fill levels of the circles indicate the subjective clarity of the observed torus signature.

the torus can be made. For T2, the situation is different and the angular width of the torus is completely contained within STEP’s FOV (Methods 5.7). We give an upper estimate for the full width of the observed torus of $\gamma \leq 20^\circ$ (see also Table 1). Thus, T2 unambiguously represents a narrow torus signature that is restricted to a small angular range. The numbers of counts that can be attributed to the observed He^+ PUI torus signatures, have been estimated by removing the respective backgrounds (pink)

of other suprathermal particles as described in Methods 5.6. From this we also derive injection times, injection path lengths, and He^+ densities which are summarized in Table 1. The related issues and interpretations are discussed further in Sect. 3.

Table 1 Observed PUI torus counts, injection times and He^+ densities.

VDF	$\frac{d\hat{C}_{\text{He}^+}}{dt}$ (1/s)	C_{He^+}	τ_{inj} (h)	L_{inj} (au)	$n_{\text{He}^+}^{\text{torus}}$ (m^{-3})	γ ($^\circ$)
T1	$2.96 \cdot 10^{-2}$	1626	15	0.22	$1.15 \cdot 10^2$	–
T2	$3.82 \cdot 10^{-2}$	3127	23	0.33	$1.72 \cdot 10^2$	≤ 20
T3	$2.77 \cdot 10^{-2}$	3492	35	0.51	$2.64 \cdot 10^2$	–

3 Implications of observed PUI properties

PUIs are continuously injected into the outward expanding solar wind plasma. As a result the in situ observed VDFs of PUIs are a complex product of the whole history of the in situ solar wind plasma, i.e. they can not be interpreted only in the context of in situ observed plasma conditions. For the observations we report on in this study the situation appears different, throughout a prolonged period of ≈ 6 hours we find torus VDFs that resemble the expectations for PUIs injected under the in situ plasma conditions.

Based on Gershman et al. [28], we conservatively expect total He^+ number densities to be in the range $10^2 \text{ m}^{-3} - 10^3 \text{ m}^{-3}$ for our period and location of interest. Compared to these reference values even our lower estimates of torus densities (see Table 1) are remarkably high. This suggests, that we observe a significant fraction of the total He^+ number density in a stable torus, which supports the inference of very weak PA scattering and hints at prolonged injection periods under very similar solar wind conditions.

Under the assumption of constant local PUI production rates, prolonged injection periods longer than ten hours (see Table 1) would be necessary to explain the observed number densities. With the in situ v_{sw} , the derived injection time periods suggest that the observed PUIs have been injected over a radial distances between 0.22 au and 0.51 au. On these spatial scales the assumption of constant neutral He number density n_{He} and should clearly be violated. In addition, the assumption that in equation 6 the quadratic scaling of the total ionization rate cancels with the quadratic scaling by expansion is also likely violated because the electron impact ionization is expected to scale differently [6, 35]. In addition, compared to EAS observations of a whole year the unusual high electron count rates shown in Fig. 1d indicate that the contribution of electron impact ionization to the total ionization rates were likely higher than assumed in Methods 5.5. However, even with a generous estimate of ten times higher electron impact ionization rates, i.e about twice as high total ionization rates, the implied injection periods are still astonishingly long.

This raises the question how such a narrow and stable torus can develop and be maintained over these scales. The identification of narrow torus VDFs directly evidences the absence of well populated shell VDFs, i.e. the PA scattering on these scales must have been very weak. To what degree an older fully scattered and already cooled PUI sphere population contributed to the non torus background or exists outside STEP’s FOV can not be concluded from the observations.

The observed narrow torus VDFs also imply that \mathbf{v}_{sw} and \mathbf{B} have been very stable on these temporal and spatial scales. Even if the direction of \mathbf{B} was stable over longer injection periods, i.e. over extended radial distances, the expansion of the plasma would lead to a decrease of B and thus to PA focusing towards field (anti-)parallel PAs. For example, the resulting PA focusing over an injection path length $L_{\text{inj}} = 0.3$, i.e. close to the value estimated for T2 in Table 1, would already have broadened the torus width by up to 36.9° (Methods 5.8). However, this is not observed in the case of T2 where the upper limit of the full width of the observed torus is only half of this expected PA broadening. This could imply a counteracting process. As mentioned in Methods 5.4, for $\text{PA} \neq 90^\circ$ the guiding center lags behind the solar wind bulk, in the case of T2 with a difference velocity $\mathbf{v}_{\text{diff}} = [40, 59, -128]$ km/s. Thus, the guiding center of these particles drift backwards, i.e. antiparallel to the magnetic field, through the observed 3D magnetic structure. In our case, this potentially leads to an accumulation of PUIs towards the end of the substructure, i.e. at about 01:30 UT in Fig. 2. As a result, the particles experienced a combination of the negative gradient of the magnetic field due to the expansion of the structure and the positive gradient within the structure. We hypothesize that these focusing processes towards and away from 90° here might have counteracted each other and stabilized the torus signature at T2.

Finally, we put the STEP observations in the context of expectations for other active PUI instruments as exemplified by the PLasma And SupraThermal Ion Composition (PLASTIC) [36] instrument of the Solar TErestrial RElations Observatory-Ahead. Unlike STEP, PLASTIC identifies ion species. However for PLASTIC this comes with the price of smaller expected PUI count rates. As derived in Methods 5.5, PLASTIC is expected to observe only $\approx 1/600$ of the PUI count rates in STEP. Thus, even the strong and long term stable torus feature filled with a high He^+ number density discussed in this study would be represented in PLASTIC by only $\approx 3\text{--}6$ counts per minute integrated over the full FOV of the solar wind section.

4 Conclusions

During an extended period of about 6 hours starting at 19:42 UT on November 4, 2021, STEP observed enhanced count rates in highly anisotropic signatures. We find that throughout this period these signatures can be clearly attributed to interstellar He^+ PUI torus VDFs that appear to have been injected under in situ observed plasma conditions. These torus VDFs are variable at a one minute time scale. We can compare our observed torus densities to expectations from local fresh injection on the one hand and on the other hand to the total He number density of all PUIs injected into the solar wind up to the spacecraft location. We find with the former that the observed torus densities are very high compared to local expectations and with the latter that

they are comparable to the total He^+ PUI number densities. Both independently imply that the observed He^+ PUIs require extended periods of PUI production, i.e. the observed He^+ PUIs have been injected over extended radial distances.

A second important observation is that the observed PA widths of the tori are narrow and thus show no evidence of significant PA scattering. In addition, the injection over such long radial distances without PA scattering should have resulted in significant broadening of the torus due to magnetic focusing from a negative B gradient in the expanding solar wind plasma. However, we find no such broadening. This in turn might point towards a more local PUI production, which would require orders of magnitude higher ionization rates than typically reported in the literature. In fact EAS observations show enhancements of suprathermal electron densities, that would result in higher local electron impact ionization rates, but the effect on the total ionization rates would be well below one order of magnitude even if the local electron impact ionization was 10 times higher. Therefore, we suggest that higher ionization rates are not sufficient to explain our observations.

In the absence of strong PA scattering, for $\text{PA} \neq 90^\circ$ the guiding center of the PUIs does not comove exactly with the solar wind bulk. Instead PUIs drift backwards through substructures which are convected with the solar wind bulk. This relative motion of the guiding center with respect to the solar wind bulk is so far not considered in typical heliospheric models which assume fully scattered VDFs [37]. In our case an observed positive gradient in the local substructure and the negative gradient due to expansion could have canceled each other out.

Our study gives the first glance of the complexities of PUI physics that have been unlocked by the unprecedented high time resolution and uninterrupted velocity space coverage of STEP. Recently, in September 2025, a state-of-the-art instrument designed for PUI measurements the Solar Wind and Pickup Ion [SWAPI; 18] Instrument on NASA's Interstellar Mapping and Acceleration Probe [IMAP; 19] was launched. Together, Solar Orbiter/EPD/STEP and IMAP/SWAPI may advance the understanding of processes related to the pickup process and VDF evolution.

Acknowledgements. Solar Orbiter is a mission of international cooperation between ESA and NASA, operated by ESA. This work was supported by the German Federal Ministry for Economic Affairs and Energy and the German Space Agency (Deutsches Zentrum für Luft- und Raumfahrt, e.V., (DLR)), grant number 50OT2002. Chaoran Gu is supported by the German Research Foundation grant number WI 2139/12-1. Verena Heidrich-Meisner is supported by DLR grant number 50OC2104.

Author contribution. R.F.W. supervised and coordinated the project, and managed funding acquisition. L.B. initiated and led the project. C.G. performed data analysis and visualizations. R.F.W. provided feedback on the initial draft. E.J., L.B. and V.H.M developed the virtual detector and provided simulation results shown in Fig. 4. C.G., E.J., L.B., and V.H.M jointly wrote the initial draft. E.J. also verified the authenticity and accuracy of all cited references. L.S. provided the 3D sketch of the instrument in Fig. 4.

Competing interests. The authors declare no competing interests.

5 Methods

5.1 Data products

For investigations of PUI VDFs, more than observations of the PUIs themselves are required. Their physical frame of reference is determined by the solar wind plasma which carries the solar magnetic field away from the Sun. In addition, electron data can provide valuable context on local ionization and thereby PUI production rates. Therefore, we use data from four instruments on Solar Orbiter [30] that are publicly available from the Solar Orbiter Archive. With the exception of the spacecraft location and the equations 2 – 8, for all measurements and derived quantities in this study we use the common coordinate system of Solar Orbiter, the spacecraft reference frame (SRF), which is illustrated in Fig. 4 a. In the SRF, the x -axis points toward the Sun.

The PUI observations we report in this study are obtained from the 1-second level 1 data of the Suprathermal Electron Proton (STEP) instrument of the Energetic Particle Detector [EPD; 29]. The STEP instrument and its data are further described in Sects. 5.2 and 5.4. Magnetic field vectors \mathbf{B} are obtained from the 8 Hz resolution data (level 2) of the Magnetometer [MAG; 38]. Solar-wind proton ground calculated moments (level 2), density n_{sw} , velocity \mathbf{v}_{sw} , and temperature T_{sw} , and energy spectra (level 1) come from the Proton-Alpha Sensor of the Solar Wind Analyser [SWA-PAS; 34] at 4-second time resolution. Solar-wind electron energy spectra (level 1) are taken from the Electron Analyser System of the Solar Wind Analyser [SWA-EAS; 34] at 10-second time resolution.

Further, we use spacecraft location and attitude information that is provided by the ESA SPICE Service [39, 40]. On the start of November 5, 2021, Solar Orbiter was at a radial distance $R = 0.85$ au, longitude $\lambda = 41.9^\circ$, and latitude $\beta = -2.0^\circ$ in ecliptic coordinates. The spacecraft was not in the focusing cone of PUIs [4–7], which is around $\lambda = 75.3^\circ$, and $\beta = -5.1^\circ$. For this location and the spacecraft orientation we calculated the expected local neutral He velocity, which is used as the local injection velocity, \mathbf{v}_{inj} , of PUIs. Therein, we assumed an ISN inflow velocity of $v_\infty = 25.4$ km/s, and an inflow direction in ecliptic coordinates of $\lambda = 75.3^\circ$, and $\beta = -5.1^\circ$. These parameters are an estimate based on the different values that are given in the literature [7, 41–51]. The temperature of ISNs and the gravitational deformation of the thermalized neutral He distribution [52] in the LISM are neglected in this study. Only the gravitational focusing and acceleration of the mean of the distribution is considered. With these values we find injection velocities in $[0.94 \pm 0.21, -21.44 \pm 0.01, -2.70 \pm 0.12]$ km/s, in the SRF on November 5, 2021. All times are given in universal time (UT).

5.2 STEP’s principle of operation

The PUI observations presented here were obtained from STEP, which was designed to measure ions and electrons at suprathermal energies. It consists of two co-aligned sensor heads with a parallel fixed field of view (FOV) of $\approx 28^\circ \times 54^\circ$ centered at the expected average Parker angle, see Fig. 4a. One of the sensor heads contains a

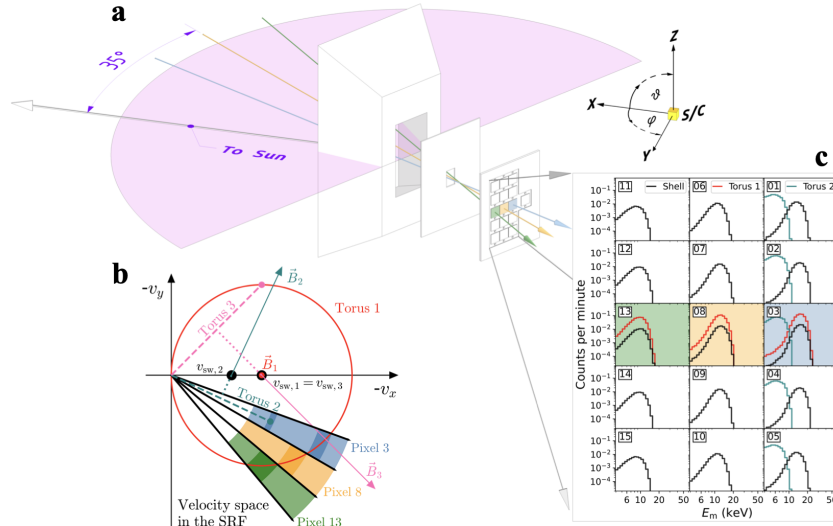


Fig. 4 |Sketch of STEP/IC, three VDFs with respect to STEP’s FOV in velocity space, and artificial measurements. **a**, Sketch of STEP/IC as a pinhole camera with three example trajectories. The SRF coordinate system is illustrated on the top right. **b**, A sketch of three torus-shaped VDFs in velocity space in SRF, and FOV of three pixels of STEP/IC. Torus 1, 2 and 3, are defined by their centers (black dots), i.e. the respective solar wind velocities $\mathbf{v}_{sw,1} = \mathbf{v}_{sw,3} = [600, 0, 0]$ km/s and $\mathbf{v}_{sw,2} = [400, 0, 0]$ km/s, and the magnetic field vectors (in red, blue and pink) with elevation angles $\vartheta_1 = 90^\circ$, $\vartheta_2 = \vartheta_3 = 0^\circ$, and azimuthal angles φ_1 (degenerate), $\varphi_2 = 245^\circ$, $\varphi_3 = 135^\circ$, respectively. The neutral He velocity is neglected in this sketch but not in the calculations. Color shaded regions indicate STEP energy ranges. **c**, Artificial energy spectra that correspond to two artificial torus VDFs and an artificial shell VDF in **b**, obtained with the virtual STEP detector described in Sect. 5.3.

permanent magnet to deflect electrons (magnet channel, MC), the other does not (integral channel, IC).

The principle of operation is depicted in Fig. 4a. Each sensor head operates as a particle pinhole camera. Particles from all directions within the FOV enter through a pinhole and are then detected by a 3×5 pixels solid-state detector [29]. In Fig. 4a, the trajectories of three example particles are shown in three colors that hit three color-shaded pixels, respectively. Each pixel views a certain direction, and the 15 pixels thus provide fine angular resolution. Within the solid-state detector, particles lose energy and the ionizing energy losses in the active volume of the detector are measured. For the main data product used in this study, the recorded energy loss of each incident particle is sorted into 32 logarithmically spaced energy bins in the range 3.92 keV - 62.72 keV. Each second for each pixel, a histogram with the number of counts per energy bin is collected. In this energy range particles are stopped in the detector and the recorded energy is a measure for their initial kinetic energy. However, due to energy losses in dead layers and non-ionizing energy losses in the active volume the fraction of the kinetic energy that is measured in the active volume of the solid state detectors is of stochastic nature and depends on the particle species, which can not be determined by STEP. For periods of enhanced suprathermal particle fluxes it is typically assumed

that protons and electrons are the dominate species. Under this assumption, the MC measures only protons, the IC protons and electrons, and electron measurements can be obtained by the difference between IC and MC. After verifying that both IC and MC show similar results for our time period of interest, in this study we only consider the IC.

The calibrated energy channels provided with the main data product are for protons with kinetic energies in the range 5.73 keV - 68.00 keV. Although He PUIs have kinetic energies in this range, this calibration cannot be used directly for He⁺ PUIs. They lose more energy in the dead layers.

5.3 Virtual STEP detector

We developed a virtual STEP detector to (1) visualize the torus and shell VDF signatures in Sect. 5.4, (2) estimate the expected number of He⁺ PUI counts and He⁺ densities in STEP in Sect. 5.5, and (3) compare observed signatures with expected signatures of PUI torus and shell VDFs in Sect. 2. The virtual STEP detector models the response function in two parts, angular responses and energy responses (both are shown in Fig. 5). For a virtual measurement, we then integrate a phase space density distribution over the combined angular and energy response function. The angular responses for the IC can be obtained by a simple geometric consideration that traces particle trajectories through the pinhole to each pixel. The energy responses of STEP's solid-state detector for He have been modeled using the GEANT4 [53] toolkit with a similar setup as for the proton responses published in the Solar Orbiter Archive. Figure 5b shows the resulting He energy responses for each energy bin. It is clearly visible that the responses are not rectangular boxes and overlap considerably. As a result, even a monoenergetic beam will be measured in several energy bins. Aging effects, e. g. growing of dead-layers on the individual pixels, are not yet included in the energy responses. Pixels 2, 3, and 4 are most affected by aging effects that effectively reduce the measured energy compared to the primary energy. Therefore, all signatures appear at lower energies in these pixels in Figs. 1, 2, and 3.

5.4 Artificial torus and shell VDFs in STEP

We use the virtual STEP detector (see Sect. 5.3) to derive signatures of expected PUI VDFs. As outlined in Sect. 1, initially PUIs form a torus VDF in the solar wind frame of reference. PA scattering then transforms these torus VDFs into shell VDFs. These VDFs are then subject to cooling or heating and ultimately lead to filled sphere VDFs. Here, we focus on the two cases that are expected to describe the VDFs of recently created PUIs, namely a torus VDF and a fully scattered shell VDF.

Figure 4b illustrates the velocity space coverage of STEP pixels 3, 8, and 12 (color shaded regions) in the v_x-v_y plane in SRF. In addition, three illustrative torus-shaped VDFs for three different magnetic field configurations and solar wind velocities are sketched. A small non-zero \mathbf{v}_{inj} of the neutral particles is omitted in the sketch, but taken into account in our analysis (see Sects. 5.1 and 2). The figure illustrates how the solar wind speed and magnetic field direction determine the position and visibility of a torus VDF in STEP's FOV.

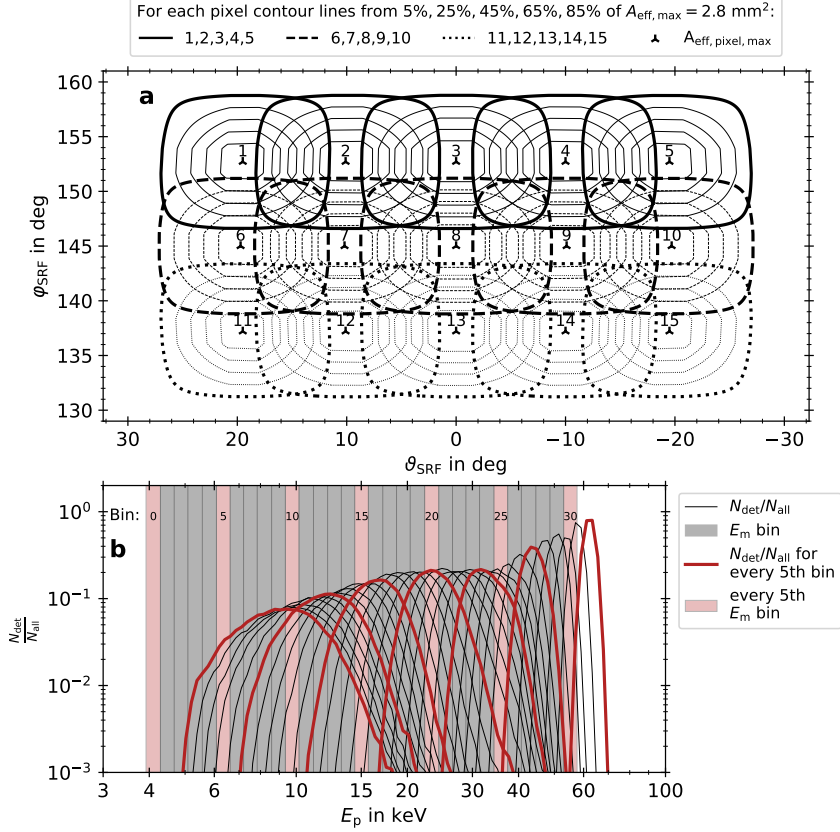


Fig. 5 Three-dimensional He response of STEP/IC. **a**, The projected effective area A_{eff} of the pinhole for each pixel in ecliptic SRF coordinates. The pixel-wise $A_{\text{eff, pixel}}$ is shown as contour lines for 5%, 25%, 45%, 65%, 85% of the global maximum $A_{\text{eff}} = 2.8 \text{ mm}^2$ which occurs in pixel 8. The contour lines for the first five pixels 1-5 are drawn with solid lines, for pixels 6-10 with dashed lines, and for pixels 11-15 with dotted lines. Each pixel is marked with the corresponding number and a ▲-symbol for the pixel-wise maxima $A_{\text{eff, pixel, max}}$. **b**, The energy calibration of STEP for He obtained from a GEANT4 simulation. It shows the fraction of detected particles, N_{det} , to the number of the injected particles, N_{all} for each primary energy E_p . This ratio shows for each of the 31 first STEP energy bins where the individual bin is sensitive in E_p with each fifth line shown in red for visibility. The shaded areas in the background indicate the positions of the 31 first STEP energy bins in measured energy E_m wherein again every fifth bin is colored red for visibility.

Torus 1 (red) is detected by all STEP pixels in the shown v_x - v_y plane but Torus 2 (teal) would only be visible in pixel 3. Torus 3 (pink) is not detected at all within STEP's FOV. Although the illustrated tori are narrow, that is, approximately monoenergetic in the solar wind frame of reference, in STEP Torus 1 and Torus 2 appear smeared out in energy on the respective pixels in SRF. This broadening of the torus signature is indicated with the darker shaded areas in Fig. 4b. In Figs. 1 and 2 the same energy uncertainty for the expected primary energy of He^+ PUIs is marked with a white-shaded band.

Figure 4c shows the resulting virtual measurements of the virtual STEP detector described in Sect. 5.3 for the same tori examples in the same respective colors as in Fig. 4b. As the input for the virtual detector, for comparability each torus VDF was filled with the same number density, that is, the same number density in position space over different volumina in velocity space, and for numerical reasons we assigned a finite full width of 20 km/s. As expected, Torus 1 is observed only by pixels 3, 8, and 12, Torus 2 is detected by pixels 1 to 5, and Torus 3 is not detected by any STEP pixel. The virtual measurements show a clear and distinct cut-off towards higher energies on the individual pixels. Therein, as expected from Fig. 4b, pixel 3 observes the torus signature at higher energies than all other pixels. On all pixels the signatures are smeared out down to the lowest observed energies. The expected geometrical broadening can also be seen in Fig. 4b (darker-color shaded regions) and is further increased by the energy responses shown in Fig. 5. From Fig. 4c we also see that the expected cut-off and broadening strongly depend on the solar wind velocity, as Torus 2 is seen at lower energies than Torus 1.

In addition, the virtual measurement of a shell VDF for the same solar wind speed, number density, and width as Torus 1 is shown in black in Fig. 4c. The shapes of the shell signatures are similar to that of the torus signatures on the pixels that also observed Torus 1, but the respective maximum count rates per pixel are about one order of magnitude smaller. In return the shell signatures are observed on all 15 pixels of STEP.

Further, we use this virtually measured shell VDF to approximate the geometrical torus broadening described above. To this end, we track the energies where the shell signatures falls to 10% of their respective maxima. These energies (calculated using the measured solar wind velocities) are marked with pairs of black lines in Fig. 1 and Fig. 2, and with pairs of dashed colored lines in Fig. 3.

Based on these considerations, we expect STEP to be able to distinguish between shell-like and torus-like VDFs. A shell VDF would be seen on all pixels and would be independent of the magnetic field direction. Whereas, under the otherwise same solar wind conditions a (narrow) torus VDF will only be observed by a few STEP pixels.

In general, the possible positions of a torus of freshly injected PUIs is restricted to a surface of a sphere in velocity space which is centered at the solar wind bulk. This is the same surface that would be fully populated by a fully scattered but not yet cooled or heated shell VDF. The radius of this shell is constructed from the solar wind velocity \mathbf{v}_{sw} and the neutral He velocity \mathbf{v}_{inj} . For a certain magnetic field direction, the position on this shell is given by its PA. Consequently, both the orientation of a PUI torus VDF and the central viewing direction of each pixel can be expressed as a PA, α_{torus} and α_{pixel} , respectively.

In the following, we derive two criteria to characterize if a torus signature of freshly injected PUIs is expected on individual STEP pixels. For the first criterion, we compare α_{torus} and α_{pixel} :

$$\Delta_{\text{PA}} = \alpha_{\text{pixel}} - \alpha_{\text{torus}}. \quad (1)$$

Thus, the respective PA difference Δ_{PA} expresses our expectation of whether a fresh, i.e. injected under the local solar wind conditions, PUI torus VDF is detectable on each individual STEP pixel. If we define the FOV of a STEP pixel as the area in

which the angular response is above 5% of its maximum, then a FOV of $\approx 10^\circ \times 15^\circ$ appears under approximately twice that angle in the solar wind frame of reference for conditions similar to Torus 1. Therefore, STEP can detect a torus VDF only on pixels with $|\Delta_{\text{PA}}| < 15^\circ$. This criterion is well suited to provide an overview of how close to the pixels' viewing direction the currently expected PUI torus is expected.

However for a tighter estimate, depending on the torus geometry, different pixels would require different thresholds. Thus, we augment Δ_{PA} with a second pixel-wise criterion that also takes the variability of the magnetic field direction into account. For a given torus, ω_{pixel} refers to the fraction of this torus that intersects with the pixel's FOV. For each magnetic field direction in 8 Hz resolution, we calculate the respective torus and then compute for each pixel the average $\tilde{\omega}_{\text{pixel}}$ over the time scale of interest, which is one minute in this study. If $\tilde{\omega}_{\text{pixel}} > 10^{-3}$ we consider this pixel to be hit during this minute, i.e. on average at least one thousandth of the torus' circumferential length intersected with the pixel's FOV. This is indicated in Fig. 3a with color-coded outlines and with a \times -symbol in Fig. 3b. Pixels that should not detect a torus signature of freshly injected He^+ PUIs are considered in the background estimation described in Sect. 5.6.

We also investigated the effect of varying v_{inj} , i.e. we calculated expected torus positions with the remote v_{inj} along the solar wind trajectory and the in situ magnetic field conditions and solar wind velocities. We found the change in the resulting α_{torus} is less than 0.5° and the change in the resulting energy is less than 0.2 keV at a radial distance of 0.85 au.

Since the STEP's FOV is oriented around the expected average Parker angle, magnetic field configurations that match Torus 1 in Fig. 4 are unusual under typical solar wind conditions and most frequently occur either in highly Alfvénic coronal hole wind or during or close to interplanetary coronal mass ejections (ICMEs).

In each torus, individual PUIs gyrate about their guiding center. For the examples in Fig. 4b, the speed of the guiding center in SRF is always below the solar wind speed. This generalizes to other PUI torus VDFs in the solar wind. The only exception are PUI VDFs with a 90° PA. Only in this case, the guiding center coincides with the solar wind bulk. As a result, after injection the guiding center typically lags behind the solar wind bulk and moves relative to the structures convected with the solar wind bulk.

5.5 Expected PUI torus VDF properties

In this section, we discuss how PUI number densities, injection time scales and injection path length can be derived from STEP observations. PUIs are injected continuously into the solar wind plasma. As a consequence, the PUI VDFs observed at a certain location have been injected over an extended time period over an extended spatial volume which contribute to a total He^+ number density, $n_{\text{He}^+}^{\text{total}}$. Information about remote plasma conditions is embedded in the VDFs. In turn, the observed VDFs can not uniquely be interpreted in the context of the locally measured plasma conditions, such as solar wind speed and magnetic field direction. If we observe torus signatures that are clearly related to the local solar wind velocity and magnetic field direction their intensity allows to estimate the temporal and spatial scales, respectively, on which the injection conditions have been stable.

We first estimate the production rate of locally produced He^+ , $\frac{dn_{\text{He}^+}}{dt}(r)$ at a radial distance r as

$$\frac{dn_{\text{He}^+}}{dt}(r) = n_{\text{He}}(r) \cdot I_{\text{He}}(r) \quad , \quad (2)$$

with position-dependent local neutral He density $n_{\text{He}}(r)$ and local total ionization rate $I_{\text{He}}(r)$. The total He^+ number density $n_{\text{He}^+}^{\text{total}}$ of all He^+ PUIs injected into a solar wind stream between a time t_0 and t with corresponding positions $r(t_0) = R_0$ and $r(t) = R$ is then obtained by integration

$$n_{\text{He}^+}^{\text{total}}(t - t_0) = \int_{t_0}^t \frac{dn_{\text{He}^+}}{dt'} \frac{r(t')^2}{R^2} dt' \quad . \quad (3)$$

The term $\frac{r(t')^2}{R^2}$ accounts for the expansion of the solar wind plasma which thins out PUIs injected further in. The time dependent position $r(t)$ is obtained by

$$r(t) = v \cdot t \quad (4)$$

with the radial velocity v . We now assume the total ionization rate to scale quadratically with the distance to the Sun, and $I_{\text{He}}(r)$ is given relative to the local total ionization rate $I_{\text{He},R}$ at a reference position R as

$$I_{\text{He}}(r) = \frac{R^2}{r^2} \cdot I_{\text{He},R} \quad . \quad (5)$$

We now assume the neutral helium density to be constant $n_{\text{He}}(r) = n_{\text{He}}$. Inserting both in the integral (equation 3) and substituting $dt = dr \cdot v^{-1}$ with a constant expansion speed v we get

$$n_{\text{He}^+}^{\text{total}}(R) = \frac{1}{v} \int_{R_0}^R n_{\text{He}} \cdot \frac{R^2}{r^2} \cdot I_{\text{He},R} \cdot \frac{r^2}{R^2} \quad dr \quad (6)$$

$$= \frac{I_{\text{He},R} \cdot n_{\text{He}}}{v} \int_{R_0}^R dr \quad (7)$$

$$= \frac{I_{\text{He},R} \cdot n_{\text{He}}}{v} (R - R_0) \quad . \quad (8)$$

And with an injection time interval $\tau_{\text{inj}} = t - t_0 = \frac{R - R_0}{v}$, the total He^+ number density is estimated as

$$n_{\text{He}^+}^{\text{total}}(\tau_{\text{inj}}) = I_{\text{He},R} \cdot n_{\text{He}} \cdot \tau_{\text{inj}} \quad , \quad (9)$$

with a corresponding injection path length $L_{\text{inj}} = R - R_0$. For the computation of L_{inj} , we assume $v = v_{\text{sw}}$.

In the following, we employ equation 9, to compute He^+ number densities and count rates. Since no reference n_{He} measurements at the same time and place are available, we use the interstellar value, $n_{\text{He}}^\infty = 1.5 \cdot 10^4 \text{ m}^{-3}$ [54, 55]. No depletion of neutral He throughout the heliosphere due to ionization is taken into account here, and thereby this value deliberately overestimates the local He density outside the focusing cone.

Solar activity dependent local total ionization rates $I_{\text{He}}(1 \text{ au})$ are derived in Sokól et al. [56]. For the period of interest we find values well below 10^{-7} s^{-1} . Again, as an overestimation we assume a rate of 10^{-7} s^{-1} at 1 au, resulting in $I_{\text{He}}(0.85 \text{ au}) = 1.4 \cdot 10^{-7} \text{ s}^{-1}$ with equation 5. With these values we obtain from equation 2 a local production rate $\frac{dn_{\text{He}^+}}{dt}(0.85 \text{ au}) = 2.1 \cdot 10^{-3} \text{ m}^{-3}\text{s}^{-1}$.

Due to their limited FOV, PUI instruments do not measure the total He^+ number density directly, but a partial number density $n_{\text{He}^+}^{\text{partial}}$. The He number density contained in the torus VDF, $n_{\text{He}^+}^{\text{torus}}$, for the magnetic field configuration represented by Torus 1 in Fig. 4 can be obtained with the fraction ω of this torus that intersects with instruments's FOV by

$$n_{\text{He}^+}^{\text{partial}} = \omega \cdot n_{\text{He}^+}^{\text{torus}} . \quad (10)$$

Then, the expected PUI production count rate, $\frac{dC_{\text{He}^+}}{dt}$, and the expected number of counts, C_{He^+} , an instrument would measure can be estimated from

$$\frac{dC_{\text{He}^+}}{dt} = v_{\text{He}^+} \cdot \tau_m \cdot \zeta \cdot A_{\text{eff}} \cdot \eta \cdot \omega \cdot n_{\text{He}}^\infty \cdot I_{\text{He},R} , \text{ and} \quad (11)$$

$$C_{\text{He}^+} = v_{\text{He}^+} \cdot \tau_m \cdot \zeta \cdot A_{\text{eff}} \cdot \eta \cdot \omega \cdot n_{\text{He}}^\infty \cdot I_{\text{He},R} \cdot \tau_{\text{inj}} . \quad (12)$$

Therein, τ_m is the measuring time interval, ζ is the duty cycle, v_{He^+} the velocity of He^+ in the SRF in the center of the FOV, A_{eff} is the FOV averaged effective area, ω is the fraction of the torus that is inside the full FOV, and η the efficiency to detect He^+ . In all following calculations we consider a fixed measuring time interval $\tau_m = 60\text{s}$. For STEP we consider $\zeta = 1$ and $\eta = 1$, i.e. all energies and directions are measured 100% of the time and He^+ is measured with 100% efficiency. The FOV averaged effective area of STEP is $A_{\text{eff}} = 2 \cdot 10^{-6} \text{ m}^2$ (compare Fig. 5). Further we assume the situation of Torus 1 shown in Fig. 4b, with $v_{\text{He}^+} = 9.83 \cdot 10^5 \text{ m/s}$ (He^+ velocity in the center of pixel 8) and the fraction $\omega = 0.156$ which corresponds to the three dark shaded areas in Fig. 4b.

Outside this section, C_{He^+} always refers to observation-derived values from STEP. \bar{C}_{He^+} refers to FOV averaged estimates following equation 12 and \hat{C}_{He^+} to estimates derived with the virtual detector.

With the values above, the expected number of counts estimated from Eq. 12 for Torus 1 measured by STEP is referred to as $\bar{C}_{\text{He}^+}^{\text{Torus } 1}$ with

$$\bar{C}_{\text{He}^+}^{\text{Torus } 1} = 0.0385 \text{ s}^{-1} \cdot \tau_{\text{inj}} . \quad (13)$$

We also estimated expected PUI production count rates $\frac{d\hat{C}_{\text{He}^+}}{dt}$ for Torus 1 and the conditions of three selected 1-minute time intervals, T1, T2, and T3, that are discussed in detail in Sect. 2.2, directly from the virtual STEP detector (Sect. 5.3). The results are given in Table 2.

For a baseline comparison to other active instruments, we also calculated expected PUI production count rates for main channel of the solar wind section of the PLasma And SupraThermal Ion Composition [PLASTIC; 36] instrument of the Solar TERrestrial RELations Observatory-Ahead (STEREO-A) which has been used in several studies. PLASTIC scans different parts of the velocity space consecutively. Therein, PLASTIC scans its FOV in 128 energy-per-charge steps and 32 deflection steps, i.e. $\zeta_{\text{PLASTIC}} = 1/128 \cdot 1/32$, within $\tau_m = 60\text{s}$, and a He^+ efficiency $\eta_{\text{PLASTIC}} \lesssim 0.5$ [36]. PLASTIC has an effective active area $A_{\text{eff,PLASTIC}} = 10^{-5}\text{m}^2$, and an intersection of the Torus 1 with its FOV $\omega_{\text{PLASTIC}} = 0.25$. The He^+ velocity at the center of the FOV $v_{\text{He}^+} = 1.2 \cdot 10^6$ m/s. This yields for the Torus 1 situation $\frac{d\overline{C}_{\text{He}^+, \text{PLASTIC}}^{\text{Torus1}}}{dt} \approx 5 \cdot 10^{-5}\text{s}^{-1}$.

As an additional reference, the expected number of counts observed by PAS for the same Torus 1 example is included in Table 2. The operation principle of PAS is similar to PLASTIC's but lacks a time-of-flight section. With a duty cycle $\zeta_{\text{PAS}} = 1/96 \cdot 1/9$, an intersection of the PAS FOV with the torus $\omega_{\text{PAS}} = 0.37$, an average effective area $A_{\text{eff,PAS}} = 4 \cdot 10^{-8}$ [57], a He^+ velocity at the center of the FOV $v_{\text{He}^+} = 1.185 \cdot 10^6$ m/s, an efficiency $\eta_{\text{PAS}} = 1$, and an integrated measurement time interval $\tau_m = 60$ s, PAS is expected to observe the He^+ production count rate $\frac{d\overline{C}_{\text{He}^+, \text{PAS}}^{\text{Torus1}}}{dt} = 3 \cdot 10^{-6}\text{s}^{-1}$. We note, that for this torus configuration, v_{He^+} in the center of PAS's FOV is already higher than the highest He^+ velocity ($\approx 9.43 \cdot 10^5$ m/s) PAS can resolve.

Table 2 Different estimates for C_{He^+} .

VDF	STEP $\frac{d\overline{C}_{\text{He}^+}}{dt}$ (1/s)	PLASTIC $\frac{d\overline{C}_{\text{He}^+}}{dt}$ (1/s)	PAS $\frac{d\overline{C}_{\text{He}^+}}{dt}$ (1/s)
Torus 1	$3.85 \cdot 10^{-2}$	$3.01 \cdot 10^{-2}$	$5 \cdot 10^{-5}$

5.6 PUI torus counts observed by STEP

From Sect. 5.5 we expect a PUI torus signature to be visible only on a subset of STEP's pixels depending on the current solar wind conditions. As described in Sect. 5.2 STEP can not discriminate different ion species. Other contributions to the observed spectra could be suprathermal tails of solar wind protons and alpha particles, solar energetic event particles, as well as PUIs with shell or sphere VDFs. Without strong assumptions about the true nature of these contributions, we take a heuristic approach to remove them.

We observe that the background in the 1 minute measurements on the individual pixels for the time period of interest shown in Sect. 2.2 is similar whenever no clear torus signature is present. Hence, in the following, we consider contributions other than the PUI torus VDFs as a constant and isotropic background for this period. So, this background does not change with time and does not depend on the magnetic field direction. With these assumptions we estimate the observed number of counts C_{He^+} in the PUI torus signatures observed in the three selected minutes, T1, T2, and T3,

investigated in Sect. 2.2. The background spectra are estimated individually for each pixel, and are defined as the average of the spectra for which no torus signature is expected under the current solar wind conditions on this pixel. For example, in Fig. 3b the background spectrum (pink) for pixel 1 is the mean spectrum of T1 (blue) and T2 (orange). The background for pixel 7 is represented by the T1 spectrum because the T2 and T3 spectra expect torus signatures.

This background estimation has some limitations. For example, as visible in Fig. 3b, in T1 the background is higher on most pixels than in T2 and T3. For another example, on pixel 8, a torus signature is visible in the STEP observations for T1, T2, and T3, although this is not expected for T1 and T3. In these cases, our background estimation is at its limit, and for example, in the case of pixel 8 by taking the average of T1 and T3 as the background spectrum, we underestimate the number of counts in the torus signature. As a result the background is likely overestimated by our approach.

With this background estimate, we can simply subtract the resulting background spectra for each pixel and obtain an estimate of the number of PUI counts C_{He^+} attributed to the torus from the respective sum over all pixel where we expect to detect a torus. Thus, the resulting observed PUI counts per minute and He^+ torus number densities are conservative lower estimates and are included in Table 1.

The He^+ torus number densities $n_{\text{He}^+}^{\text{torus}}$, the injection path lengths L_{inj} , and the injection times τ_{inj} are discussed in Sect. 3.

5.7 PUI torus width observed by STEP

As visible in Fig. 3, in time period T2 the observed torus signatures are confined within STEP's FOV. Pixels 1 and 6 that look at PAs smaller than the expected torus PAs and pixels 10 and 15 that look at PAs larger than the expected torus PAs observe no torus signatures. Among these pixels, Fig. 3 shows that the lower right edge of pixel 6 and the upper left edge of pixel 10, respectively, look closest to the expected torus positions. Therefore, we take the sum of the minima of the absolute PA difference of these two pixels and the expected tori PAs within T2 plus the spread of the expected torus PAs as an upper estimate for the full width, γ , of the observed torus signature (see Tab. 1). We emphasize that this is a loose upper limit and any larger width would not be consistent with the STEP observations.

5.8 Pitch Angle focusing

From the conservation of the magnetic moment of charged particles follows a change of the particles' PA if the magnetic field strength B changes. The resulting PA α_2 can be calculated from the original PA α_1 if the magnetic field changed from B_1 to B_2 by

$$\alpha_2 = \arcsin \left(\sin(\alpha_1) \cdot \sqrt{\frac{B_2}{B_1}} \right). \quad (14)$$

In the outward expanding solar wind plasma B is expected to decrease radially and thus the PA α_{inj} of PUIs that have been injected closer to the Sun should have changed according to equation 14 towards the parallel or anti parallel direction, for $\alpha_{\text{inj}} < 90^\circ$

and $\alpha_{\text{inj}} > 90^\circ$, respectively. Close to the Sun, the magnetic field is expected to decrease with r^{-2} [58]. Thereby we can calculate the expected PA changes of PUIs that have been injected in the history of the in situ plasma (see Eq. 3).

For the situation in T2 (see Sect. 2.2), this focusing effect can be quantified as follows. For a distance of $L_{\text{inj}} = 0.1$ au ($L_{\text{inj}} = 0.3$ au), i.e. PUIs that have been injected at $r = 0.75$ au ($r = 0.55$ au), at $\alpha_{\text{inj}} = 104.2^\circ$, i.e. the in situ observed conditions in T2, we obtain an in situ PA $\alpha_{\text{in situ}} = 121.2^\circ$ ($\alpha_{\text{in situ}} = 141.1^\circ$). Thus, the contribution of the PUIs to the joined VDF that have been injected further in should have broadened the torus VDF significantly in PA from $\alpha_{\text{inj}} = 104.2^\circ$ towards 180° for the injection path lengths $L_{\text{inj}} = 0.33$ (see Table 1).

References

- [1] Parker, E.N.: The Stellar-Wind Regions. ApJ **134**, 20 (1961) <https://doi.org/10.1086/147124>
- [2] Cox, D.P., Reynolds, R.J.: The local interstellar medium. ARA&A **25**, 303–344 (1987) <https://doi.org/10.1146/annurev.aa.25.090187.001511>
- [3] Sokół, J.M., Bzowski, M., Tokumaru, M.: Interstellar Neutral Gas Species and Their Pickup Ions inside the Heliospheric Termination Shock. Ionization Rates for H, O, Ne, and He. ApJ **872**(1), 57 (2019) <https://doi.org/10.3847/1538-4357/aafdaf> [arXiv:1809.09823](https://arxiv.org/abs/1809.09823) [physics.space-ph]
- [4] Fahr, H.J.: Charge-transfer Interactions between Solar Wind Protons and Neutral Particles in the Vicinity of the Sun. Nature **219**(5153), 473–474 (1968) <https://doi.org/10.1038/219473a0>
- [5] Möbius, E., Rucinski, D., Hovestadt, D., Klecker, B.: The helium parameters of the very local interstellar medium as derived from the distribution of He⁺ pickup ions in the solar wind. A&A **304**, 505 (1995)
- [6] Gloeckler, G., Möbius, E., Geiss, J., Bzowski, M., Chalov, S., Fahr, H., McMullin, D.R., Noda, H., Oka, M., Ruciński, D., Skoug, R., Terasawa, T., von Steiger, R., Yamazaki, A., Zurbuchen, T.: Observations of the helium focusing cone with pickup ions. A&A **426**, 845–854 (2004) <https://doi.org/10.1051/0004-6361:20035768>
- [7] Drews, C., Berger, L., Wimmer-Schweingruber, R.F., Bochsler, P., Galvin, A.B., Klecker, B., Möbius, E.: Inflow direction of interstellar neutrals deduced from pickup ion measurements at 1 AU. Journal of Geophysical Research (Space Physics) **117**(A9), 09106 (2012) <https://doi.org/10.1029/2012JA017746>
- [8] Möbius, E., Hovestadt, D., Klecker, B., Scholer, M., Gloeckler, G., Ipavich, F.M.: Direct observation of He⁺ pick-up ions of interstellar origin in the solar wind. Nature **318**(6045), 426–429 (1985) <https://doi.org/10.1038/318426a0>

- [9] Burlaga, L.F., Ness, N.F., Belcher, J.W., Whang, Y.C.: Pickup protons and pressure-balanced structures from 39 to 43 AU: Voyager 2 observations during 1993 and 1994. *J. Geophys. Res.* **101**(A7), 15523–15254 (1996) <https://doi.org/10.1029/96JA01076>
- [10] Sokół, J.M., Kucharek, H., Baliukin, I.I., Fahr, H., Izmodenov, V.V., Kornbleuth, M., Mostafavi, P., Opher, M., Park, J., Pogorelov, N.V., Quinn, P.R., Smith, C.W., Zank, G.P., Zhang, M.: Interstellar Neutrals, Pickup Ions, and Energetic Neutral Atoms Throughout the Heliosphere: Present Theory and Modeling Overview. *Space Sci. Rev.* **218**(3), 18 (2022) <https://doi.org/10.1007/s11214-022-00883-6>
- [11] McComas, D.J., Schwadron, N.A., Crary, F.J., Elliott, H.A., Young, D.T., Gosling, J.T., Thomsen, M.F., Sittler, E., Berthelier, J.-J., Szego, K., Coates, A.J.: The interstellar hydrogen shadow: Observations of interstellar pickup ions beyond Jupiter. *Journal of Geophysical Research (Space Physics)* **109**(A2), 02104 (2004) <https://doi.org/10.1029/2003JA010217>
- [12] Bzowski, M., Sokół, J.M., Kubiak, M.A., Kucharek, H.: Modulation of neutral interstellar He, Ne, O in the heliosphere. Survival probabilities and abundances at IBEX. *A&A* **557**, 50 (2013) <https://doi.org/10.1051/0004-6361/201321700> [arXiv:1306.4463](https://arxiv.org/abs/1306.4463) [astro-ph.IM]
- [13] Kowalska-Leszczynska, I., Kubiak, M.A., Bzowski, M.: Radiation Pressure Acting on the Neutral He Atoms in the Heliosphere. *ApJ* **950**(2), 98 (2023) <https://doi.org/10.3847/1538-4357/acd18f> [arXiv:2305.04510](https://arxiv.org/abs/2305.04510) [astro-ph.GA]
- [14] Zirnstein, E.J., Möbius, E., Zhang, M., Bower, J., Elliott, H.A., McComas, D.J., Pogorelov, N.V., Swaczyna, P.: In Situ Observations of Interstellar Pickup Ions from 1 au to the Outer Heliosphere. *Space Sci. Rev.* **218**(4), 28 (2022) <https://doi.org/10.1007/s11214-022-00895-2>
- [15] Vasyliunas, V.M., Siscoe, G.L.: On the flux and the energy spectrum of interstellar ions in the solar system. *J. Geophys. Res.* **81**(7), 1247 (1976) <https://doi.org/10.1029/JA081i007p01247>
- [16] Isenberg, P.A.: Interaction of the solar wind with interstellar neutral hydrogen: three-fluid model. *J. Geophys. Res.* **91**(A9), 9965–9972 (1986) <https://doi.org/10.1029/JA091iA09p09965>
- [17] Moebius, E., Klecker, B., Hovestadt, D., Scholer, M.: Interaction of Interstellar Pick-Up Ions with the Solar Wind. *Ap&SS* **144**(1-2), 487–505 (1988) <https://doi.org/10.1007/BF00793200>
- [18] Rankin, J.S., McComas, D.J., Alimaganbetov, M., Angold, N., Dunn, G.F., Elliott, H.A., Everett, D., Escobar, J.D., Galvin, M.B., Khoo, L.Y., Letzer, J.T., Roemer, E.M., Savage, B., Shaw-Lecarf, M., Shen, M.M., Shrestha, B.L.,

- Teifert, J., Weidner, S.E., Zirnstein, E.J., Christian, E.R., Gkioulidou, M., Nicolaou, G., Schwadron, N.A., Swaczyna, P., Tapley, M.B.: Solar Wind and Pickup Ion (SWAPI) Instrument on NASA’s Interstellar Mapping and Acceleration Probe (IMAP). *Space Sci. Rev.* **221**(8), 108 (2025) <https://doi.org/10.1007/s11214-025-01229-8>
- [19] McComas, D.J., Christian, E.R., Schwadron, N.A., Gkioulidou, M., Allegrini, F., Baker, D.N., Bzowski, M., Clark, G., Cohen, C.M.S., Cohen, I., Collura, C., Cully, M.J., Dalla, S., Desai, M.I., Driesman, A., Eng, D., Fox, N.J., Funsten, H.O., Fuselier, S.A., Galli, A., Giacalone, J., Hahn, J., Hegarty, K.P., Horbury, T., Horanyi, M., Kistler, L.M., Kubiak, M.A., Kubota, S., Livi, S., Lugaz, N., Lee, C.O., Luhmann, J., Matthaeus, W., Mitchell, D.G., Mitchell, J.G., Moebius, E., Pope, S., Provornikova, E., Rankin, J.S., Reisenfeld, D.B., Reno, C., Richardson, J.D., Russell, C.T., Shaw-Lecarf, M.M., Scherrer, J., Skoug, R.M., Shen, M.M., Spence, H.E., Sternovsky, Z., Strumik, M., Szalay, J.R., Tapley, M., Tokumaru, M., Turner, D.L., Weidner, S., Westlake, J., Wurz, P., Zank, G.P.: Interstellar Mapping And Acceleration Probe: The NASA IMAP Mission. *Space Sci. Rev.* **221**(8), 100 (2025) <https://doi.org/10.1007/s11214-025-01224-z>
- [20] Oka, M., Terasawa, T., Noda, H., Saito, Y., Mukai, T.: ‘Torus’ distribution of interstellar helium pickup ions: Direct observation. *Geophys. Res. Lett.* **29**(12), 1612 (2002) <https://doi.org/10.1029/2002GL015111>
- [21] Drews, C., Berger, L., Taut, A., Peleikis, T., Wimmer-Schweingruber, R.F.: 2D He⁺ pickup ion velocity distribution functions: STEREO PLASTIC observations. *A&A* **575**, 97 (2015) <https://doi.org/10.1051/0004-6361/201425271>
- [22] Starkey, M., Fuselier, S.A., Desai, M.I., Schwartz, S.J., Gomez, R.G., Mukherjee, J., Cohen, I.J., Russell, C.T.: MMS Observations of Accelerated Interstellar Pickup He⁺ Ions at an Interplanetary Shock. *ApJ* **897**(1), 6 (2020) <https://doi.org/10.3847/1538-4357/ab960c>
- [23] Ogasawara, K., Dayeh, M.A., Ebert, R.W., Klecker, B., Kucharek, H.: Helium Pickup Ion Velocity Distributions Observed in Interplanetary Coronal Mass Ejection Structures. *ApJ* **981**(1), 35 (2025) <https://doi.org/10.3847/1538-4357/adb1b4>
- [24] Möbius, E.: Pick-up of interstellar neutrals by the solar wind. *Advances in Space Research* **6**(1), 199–208 (1986) [https://doi.org/10.1016/0273-1177\(86\)90034-7](https://doi.org/10.1016/0273-1177(86)90034-7)
- [25] Keilbach, D., Heidrich-Meisner, V., Berger, L., Wimmer-Schweingruber, R.F.: Three-dimensional He⁺ pick-up ion velocity distribution functions observed with STEREO-A PLASTIC. *A&A* **696**, 115 (2025) <https://doi.org/10.1051/0004-6361/202453527> [arXiv:2503.10936](https://arxiv.org/abs/2503.10936) [astro-ph.SR]
- [26] Möbius, E., Litvinenko, Y., Grüwaldt, H., Aellig, M.R., Bogdanov, A., Ipavich, F.M., Bochsler, P., Hilchenbach, M., Judge, D., Klecker, B., Lee, M.A., Ogawa,

- H.: Direct evidence of the interstellar gas flow velocity in the pickup ion cut-off as observed with SOHO CELIAS CTOF. *Geophys. Res. Lett.* **26**(20), 3181–3184 (1999) <https://doi.org/10.1029/1999GL003644>
- [27] Gloeckler, G., Geiss, J.: Interstellar and Inner Source Pickup Ions Observed with SWICS on ULYSSES. *Space Sci. Rev.* **86**, 127–159 (1998) <https://doi.org/10.1023/A:1005019628054>
- [28] Gershman, D.J., Gloeckler, G., Gilbert, J.A., Raines, J.M., Fisk, L.A., Solomon, S.C., Stone, E.C., Zurbuchen, T.H.: Observations of interstellar helium pickup ions in the inner heliosphere. *Journal of Geophysical Research (Space Physics)* **118**(4), 1389–1402 (2013) <https://doi.org/10.1002/jgra.50227>
- [29] Rodríguez-Pacheco, J., Wimmer-Schweingruber, R.F., Mason, G.M., Ho, G.C., Sánchez-Prieto, S., Prieto, M., Martín, C., Seifert, H., Andrews, G.B., Kulkarni, S.R., Panitzsch, L., Boden, S., Böttcher, S.I., Cernuda, I., Elftmann, R., Espinosa Lara, F., Gómez-Herrero, R., Terasa, C., Almena, J., Begley, S., Böhm, E., Blanco, J.J., Boogaerts, W., Carrasco, A., Castillo, R., da Silva Fariña, A., de Manuel González, V., Drews, C., Dupont, A.R., Eldrum, S., Gordillo, C., Gutiérrez, O., Haggerty, D.K., Hayes, J.R., Heber, B., Hill, M.E., Jüngling, M., Kerem, S., Knierim, V., Köhler, J., Kolbe, S., Kulemzin, A., Lario, D., Lees, W.J., Liang, S., Martínez Hellín, A., Meziat, D., Montalvo, A., Nelson, K.S., Parra, P., Paspirgilis, R., Ravanbakhsh, A., Richards, M., Rodríguez-Polo, O., Russu, A., Sánchez, I., Schlemm, C.E., Schuster, B., Seimetz, L., Steinhagen, J., Tammen, J., Tyagi, K., Varela, T., Yedla, M., Yu, J., Agueda, N., Aran, A., Horbury, T.S., Klecker, B., Klein, K.-L., Kontar, E., Krucker, S., Maksimovic, M., Malandraki, O., Owen, C.J., Pacheco, D., Sanahuja, B., Vainio, R., Connell, J.J., Dalla, S., Dröge, W., Gevin, O., Gopalswamy, N., Kartavykh, Y.Y., Kudela, K., Limousin, O., Makela, P., Mann, G., Önel, H., Posner, A., Ryan, J.M., Soucek, J., Hofmeister, S., Vilmer, N., Walsh, A.P., Wang, L., Wiedenbeck, M.E., Wirth, K., Zong, Q.: The Energetic Particle Detector. Energetic particle instrument suite for the Solar Orbiter mission. *A&A* **642**, 7 (2020) <https://doi.org/10.1051/0004-6361/201935287>
- [30] Müller, D., St. Cyr, O.C., Zouganelis, I., Gilbert, H.R., Marsden, R., Nieves-Chinchilla, T., Antonucci, E., Auchère, F., Berghmans, D., Horbury, T.S., Howard, R.A., Krucker, S., Maksimovic, M., Owen, C.J., Rochus, P., Rodríguez-Pacheco, J., Romoli, M., Solanki, S.K., Bruno, R., Carlsson, M., Fludra, A., Harra, L., Hassler, D.M., Livi, S., Louarn, P., Peter, H., Schühle, U., Teriaca, L., del Toro Iniesta, J.C., Wimmer-Schweingruber, R.F., Marsch, E., Velli, M., De Groof, A., Walsh, A., Williams, D.: The Solar Orbiter mission. Science overview. *A&A* **642**, 1 (2020) <https://doi.org/10.1051/0004-6361/202038467> arXiv:2009.00861 [astro-ph.SR]
- [31] Nieves-Chinchilla, T., Linton, M.G., Hidalgo, M.A., Vourlidas, A., Savani, N.P., Szabo, A., Farrugia, C., Yu, W.: A Circular-cylindrical Flux-rope Analytical Model for Magnetic Clouds. *ApJ* **823**(1), 27 (2016) <https://doi.org/10.3847/>

- [32] Trotta, D., Hietala, H., Horbury, T., Dresing, N., Vainio, R., Wilson, L., Plotnikov, I., Kilpua, E.: Multi-spacecraft observations of shocklets at an interplanetary shock. *MNRAS* **520**(1), 437–445 (2023) <https://doi.org/10.1093/mnras/stad104> [arXiv:2209.13544](https://arxiv.org/abs/2209.13544) [physics.space-ph]
- [33] Wimmer-Schweingruber, R.F., Crooker, N.U., Balogh, A., Bothmer, V., Forsyth, R.J., Gazis, P., Gosling, J.T., Horbury, T., Kilchenmann, A., Richardson, I.G., Richardson, J.D., Riley, P., Rodriguez, L., von Steiger, R., Wurz, P., Zurbuchen, T.H.: Understanding Interplanetary Coronal Mass Ejection Signatures. Report of Working Group B. *Space Sci. Rev.* **123**(1-3), 177–216 (2006) <https://doi.org/10.1007/s11214-006-9017-x>
- [34] Owen, C.J., Bruno, R., Livi, S., Louarn, P., Al Janabi, K., Allegrini, F., Amoros, C., Baruah, R., Barthe, A., Berthomier, M., Bordon, S., Brockley-Blatt, C., Brysbaert, C., Capuano, G., Collier, M., DeMarco, R., Fedorov, A., Ford, J., Fortunato, V., Fratter, I., Galvin, A.B., Hancock, B., Heirtzler, D., Kataria, D., Kistler, L., Lepri, S.T., Lewis, G., Loeffler, C., Marty, W., Mathon, R., Mayall, A., Mele, G., Ogasawara, K., Orlandi, M., Pacros, A., Penou, E., Persyn, S., Petiot, M., Phillips, M., Přeč, L., Raines, J.M., Reden, M., Rouillard, A.P., Rousseau, A., Rubiella, J., Seran, H., Spencer, A., Thomas, J.W., Trevino, J., Verscharen, D., Wurz, P., Alapide, A., Amoruso, L., André, N., Anekallu, C., Arciuli, V., Arnett, K.L., Ascolese, R., Bancroft, C., Bland, P., Brysch, M., Calvanese, R., Castronuovo, M., Čermák, I., Chornay, D., Clemens, S., Coker, J., Collinson, G., D’Amicis, R., Dandouras, I., Darnley, R., Davies, D., Davison, G., De Los Santos, A., Devoto, P., Dirks, G., Edlund, E., Fazakerley, A., Ferris, M., Frost, C., Fruit, G., Garat, C., Génot, V., Gibson, W., Gilbert, J.A., de Giosa, V., Gradone, S., Hailey, M., Horbury, T.S., Hunt, T., Jacquy, C., Johnson, M., Lavraud, B., Lawrenson, A., Leblanc, F., Lockhart, W., Maksimovic, M., Malpus, A., Marcucci, F., Mazelle, C., Monti, F., Myers, S., Nguyen, T., Rodriguez-Pacheco, J., Phillips, I., Popecki, M., Rees, K., Rogacki, S.A., Ruane, K., Rust, D., Salatti, M., Sauvaud, J.A., Stakhiv, M.O., Stange, J., Stubbs, T., Taylor, T., Techer, J.-D., Terrier, G., Thibodeaux, R., Urdiales, C., Varsani, A., Walsh, A.P., Watson, G., Wheeler, P., Willis, G., Wimmer-Schweingruber, R.F., Winter, B., Yardley, J., Zouganelis, I.: The Solar Orbiter Solar Wind Analyser (SWA) suite. *Astronomy and Astrophysics* **642**, 16 (2020) <https://doi.org/10.1051/0004-6361/201937259>
- [35] Rucinski, D., Fahr, H.J.: The influence of electron impact ionization on the distribution of interstellar helium in the inner heliosphere - Possible consequences for determination of interstellar helium parameters. *A&A* **224**(1-2), 290–298 (1989)
- [36] Galvin, A.B., Kistler, L.M., Popecki, M.A., Farrugia, C.J., Simunac, K.D.C., Ellis, L., Möbius, E., Lee, M.A., Boehm, M., Carroll, J., Crawshaw, A., Conti, M., Demaine, P., Ellis, S., Gaidos, J.A., Googins, J., Granoff, M., Gustafson, A., Heirtzler, D., King, B., Knauss, U., Levasseur, J., Longworth, S., Singer, K., Turco,

- S., Vachon, P., Vosbury, M., Widholm, M., Blush, L.M., Karrer, R., Bochsler, P., Daoudi, H., Etter, A., Fischer, J., Jost, J., Opitz, A., Sigrist, M., Wurz, P., Klecker, B., Ertl, M., Seidenschwang, E., Wimmer-Schweingruber, R.F., Koeten, M., Thompson, B., Steinfeld, D.: The Plasma and Suprathermal Ion Composition (PLASTIC) Investigation on the STEREO Observatories. *Space Sci. Rev.* **136**(1-4), 437–486 (2008) <https://doi.org/10.1007/s11214-007-9296-x>
- [37] Cohen, C.M.S., Alterman, B.L., Baker, D.N., Bruno, A., Bzowski, M., Christian, E.R., Cohen, I.J., Dalla, S., Dayeh, M.A., Desai, M.I., Elliott, H.A., Giacalone, J., Gkioulidou, M., Guo, F., Horbury, T., Kanekal, S.G., Kowalska-Leszczynska, I., Lee, C.O., Livadiotis, G.I., Luhmann, J.G., Matthaeus, W.H., McComas, D.J., Mitchell, J.G., Moebius, E., Rankin, J., Richardson, J.D., Schwadron, N.A., Skoug, R., Turner, D., Zank, G., Zirnstein, E.J.: IMAP’s Role in Understanding Particle Injection and Energization Throughout the Heliosphere. *Space Sci. Rev.* **222**(1), 6 (2026) <https://doi.org/10.1007/s11214-025-01257-4>
- [38] Horbury, T.S., O’Brien, H., Carrasco Blazquez, I., Bendyk, M., Brown, P., Hudson, R., Evans, V., Oddy, T.M., Carr, C.M., Beek, T.J., Cupido, E., Bhattacharya, S., Dominguez, J.-A., Matthews, L., Myklebust, V.R., Whiteside, B., Bale, S.D., Baumjohann, W., Burgess, D., Carbone, V., Cargill, P., Eastwood, J., Erdős, G., Fletcher, L., Forsyth, R., Giacalone, J., Glassmeier, K.-H., Goldstein, M.L., Hoeksema, T., Lockwood, M., Magnes, W., Maksimovic, M., Marsch, E., Matthaeus, W.H., Murphy, N., Nakariakov, V.M., Owen, C.J., Owens, M., Rodriguez-Pacheco, J., Richter, I., Riley, P., Russell, C.T., Schwartz, S., Vainio, R., Velli, M., Vennerstrom, S., Walsh, R., Wimmer-Schweingruber, R.F., Zank, G., Müller, D., Zouganelis, I., Walsh, A.P.: The Solar Orbiter magnetometer. *A&A* **642**, 9 (2020) <https://doi.org/10.1051/0004-6361/201937257>
- [39] Acton, C.H.: Ancillary data services of NASA’s Navigation and Ancillary Information Facility. *Planet. Space Sci.* **44**(1), 65–70 (1996) [https://doi.org/10.1016/0032-0633\(95\)00107-7](https://doi.org/10.1016/0032-0633(95)00107-7)
- [40] Acton, C., Bachman, N., Semenov, B., Wright, E.: A look towards the future in the handling of space science mission geometry. *Planet. Space Sci.* **150**, 9–12 (2018) <https://doi.org/10.1016/j.pss.2017.02.013>
- [41] Witte, M.: Kinetic parameters of interstellar neutral helium. Review of results obtained during one solar cycle with the Ulysses/GAS-instrument. *A&A* **426**, 835–844 (2004) <https://doi.org/10.1051/0004-6361:20035956>
- [42] McComas, D.J., Alexashov, D., Bzowski, M., Fahr, H., Heerikhuisen, J., Izmodenov, V., Lee, M.A., Möbius, E., Pogorelov, N., Schwadron, N.A., Zank, G.P.: The Heliosphere’s Interstellar Interaction: No Bow Shock. *Science* **336**(6086), 1291 (2012) <https://doi.org/10.1126/science.1221054>
- [43] Bzowski, M., Kubiak, M.A., Möbius, E., Bochsler, P., Leonard, T., Heirtzler, D., Kucharek, H., Sokół, J.M., Hłond, M., Crew, G.B., Schwadron, N.A., Fuselier,

- S.A., McComas, D.J.: Neutral Interstellar Helium Parameters Based on IBEX-Lo Observations and Test Particle Calculations. *ApJS* **198**(2), 12 (2012) <https://doi.org/10.1088/0067-0049/198/2/12> arXiv:1202.0415 [astro-ph.GA]
- [44] Möbius, E., Bochsler, P., Bzowski, M., Heirtzler, D., Kubiak, M.A., Kucharek, H., Lee, M.A., Leonard, T., Schwadron, N.A., Wu, X., Fuselier, S.A., Crew, G., McComas, D.J., Petersen, L., Saul, L., Valocin, D., Vanderspek, R., Wurz, P.: Interstellar Gas Flow Parameters Derived from Interstellar Boundary Explorer-Lo Observations in 2009 and 2010: Analytical Analysis. *ApJS* **198**(2), 11 (2012) <https://doi.org/10.1088/0067-0049/198/2/11>
- [45] Bzowski, M., Kubiak, M.A., Hłond, M., Sokół, J.M., Banaszekiewicz, M., Witte, M.: Neutral interstellar He parameters in front of the heliosphere 1994-2007. *A&A* **569**, 8 (2014) <https://doi.org/10.1051/0004-6361/201424127> arXiv:1405.0623 [astro-ph.SR]
- [46] Wood, B.E., Müller, H.-R., Witte, M.: Revisiting Ulysses Observations of Interstellar Helium. *ApJ* **801**(1), 62 (2015) <https://doi.org/10.1088/0004-637X/801/1/62> arXiv:1501.02725 [astro-ph.SR]
- [47] McComas, D.J., Bzowski, M., Frisch, P., Fuselier, S.A., Kubiak, M.A., Kucharek, H., Leonard, T., Möbius, E., Schwadron, N.A., Sokół, J.M., Swaczyna, P., Witte, M.: Warmer Local Interstellar Medium: A Possible Resolution of the Ulysses-IBEX Enigma. *ApJ* **801**(1), 28 (2015) <https://doi.org/10.1088/0004-637X/801/1/28>
- [48] Leonard, T.W., Möbius, E., Bzowski, M., Fuselier, S.A., Heirtzler, D., Kubiak, M.A., Kucharek, H., Lee, M.A., McComas, D.J., Schwadron, N.A., Wurz, P.: Revisiting the ISN Flow Parameters, Using a Variable IBEX Pointing Strategy. *ApJ* **804**(1), 42 (2015) <https://doi.org/10.1088/0004-637X/804/1/42>
- [49] Bzowski, M., Swaczyna, P., Kubiak, M.A., Sokół, J.M., Fuselier, S.A., Galli, A., Heirtzler, D., Kucharek, H., Leonard, T.W., McComas, D.J., Möbius, E., Schwadron, N.A., Wurz, P.: Interstellar Neutral Helium in the Heliosphere from IBEX Observations. III. Mach Number of the Flow, Velocity Vector, and Temperature from the First Six Years of Measurements. *ApJS* **220**(2), 28 (2015) <https://doi.org/10.1088/0067-0049/220/2/28> arXiv:1510.04835 [astro-ph.SR]
- [50] Taut, A., Berger, L., Möbius, E., Drews, C., Heidrich-Meisner, V., Keilbach, D., Lee, M.A., Wimmer-Schweingruber, R.F.: Challenges in the determination of the interstellar flow longitude from the pickup ion cutoff. *A&A* **611**, 61 (2018) <https://doi.org/10.1051/0004-6361/201731796>
- [51] Swaczyna, P., Bzowski, M., Heerikhuisen, J., Kubiak, M.A., Rahmanifard, F., Zirnstein, E.J., Fuselier, S.A., Galli, A., McComas, D.J., Möbius, E., Schwadron, N.A.: Interstellar Conditions Deduced from Interstellar Neutral Helium Observed by IBEX and Global Heliosphere Modeling. *ApJ* **953**(1), 107 (2023) <https://doi.org/10.1088/1538-4357/acbc00>

- [52] Müller, H.-R., Cohen, J.H.: Primary neutral helium in the heliosphere. In: Heerikhuisen, J., Li, G., Pogorelov, N., Zank, G. (eds.) *Physics of the Heliosphere: A 10 Year Retrospective*. American Institute of Physics Conference Series, vol. 1436, pp. 233–238. AIP, Melville, NY (2012). <https://doi.org/10.1063/1.4723613>
- [53] Agostinelli, S., Allison, J., Amako, K., Apostolakis, J., Araujo, H., Arce, P., Asai, M., Axen, D., Banerjee, S., Barrand, G., Behner, F., Bellagamba, L., Boudreau, J., Broglia, L., Brunengo, A., Burkhardt, H., Chauvie, S., Chuma, J., Chytráček, R., Cooperman, G., Cosmo, G., Degtyarenko, P., Dell’Acqua, A., Depaola, G., Dietrich, D., Enami, R., Feliciello, A., Ferguson, C., Fesefeldt, H., Folger, G., Foppiano, F., Forti, A., Garelli, S., Giani, S., Giannitrapani, R., Gibin, D., Gómez Cadenas, J.J., González, I., Gracia Abril, G., Greeniaus, G., Greiner, W., Grichine, V., Grossheim, A., Guatelli, S., Gumplinger, P., Hamatsu, R., Hashimoto, K., Hasui, H., Heikkinen, A., Howard, A., Ivanchenko, V., Johnson, A., Jones, F.W., Kallenbach, J., Kanaya, N., Kawabata, M., Kawabata, Y., Kawaguti, M., Kelner, S., Kent, P., Kimura, A., Kodama, T., Kokoulin, R., Kossov, M., Kurashige, H., Lamanna, E., Lampén, T., Lara, V., Lefebvre, V., Lei, F., Liendl, M., Lockman, W., Longo, F., Magni, S., Maire, M., Medernach, E., Minamimoto, K., Mora de Freitas, P., Morita, Y., Murakami, K., Nagamatsu, M., Nartallo, R., Nieminen, P., Nishimura, T., Ohtsubo, K., Okamura, M., O’Neale, S., Oohata, Y., Paech, K., Perl, J., Pfeiffer, A., Pia, M.G., Ranjard, F., Rybin, A., Sadilov, S., Di Salvo, E., Santin, G., Sasaki, T., Savvas, N., Sawada, Y., Scherer, S., Sei, S., Sirotenko, V., Smith, D., Starkov, N., Stoecker, H., Sulkimo, J., Takahata, M., Tanaka, S., Tcherniaev, E., Safai Tehrani, E., Tropeano, M., Truscott, P., Uno, H., Urban, L., Urban, P., Verderi, M., Walkden, A., Wander, W., Weber, H., Wellisch, J.P., Wenaus, T., Williams, D.C., Wright, D., Yamada, T., Yoshida, H., Zschesche, D., G EANT4 Collaboration: GEANT4—a simulation toolkit. *Nuclear Instruments and Methods in Physics Research A* **506**(3), 250–303 (2003) [https://doi.org/10.1016/S0168-9002\(03\)01368-8](https://doi.org/10.1016/S0168-9002(03)01368-8)
- [54] Bzowski, M., Czechowski, A., Frisch, P.C., Fuselier, S.A., Galli, A., Grygorczuk, J., Heerikhuisen, J., Kubiak, M.A., Kucharek, H., McComas, D.J., Möbius, E., Schwadron, N.A., Slavin, J., Sokół, J.M., Swaczyna, P., Wurz, P., Zirnstein, E.J.: Interstellar Neutral Helium in the Heliosphere from IBEX Observations. VI. The He⁺ Density and the Ionization State in the Very Local Interstellar Matter. *ApJ* **882**(1), 60 (2019) <https://doi.org/10.3847/1538-4357/ab3462> arXiv:1907.09645 [astro-ph.SR]
- [55] Islam, H., Schwadron, N.A., Möbius, E., Rahmanifard, F., Sokół, J.M., Galli, A., McComas, D.J., Wurz, P., Fuselier, S.A., Fairchild, K.W., Heirtzler, D.: IBEX Observations of Elastic Scattering of Interstellar Helium by Solar Wind Particles. *ApJ* **991**(2), 122 (2025) <https://doi.org/10.3847/1538-4357/adf4cc> arXiv:2409.11784 [astro-ph.SR]

- [56] Sokół, J.M., Kubiak, M.A., Bzowski, M., Swaczyna, P.: Interstellar Neutral Helium in the Heliosphere from IBEX Observations. II. The Warsaw Test Particle Model (WTPM). *ApJS* **220**(2), 27 (2015) <https://doi.org/10.1088/0067-0049/220/2/27> [arXiv:1510.04869](https://arxiv.org/abs/1510.04869) [astro-ph.SR]
- [57] Berger, L., Heidrich-Meisner, V., Kühl, P., Fedorov, A., Jentsch, E., Louarn, P., Wimmer-Schweingruber, R.F.: Solar wind temperature measurements. *A&A* **702**, 135 (2025) <https://doi.org/10.1051/0004-6361/202555609>
- [58] Owens, M.J., Forsyth, R.J.: The Heliospheric Magnetic Field. *Living Reviews in Solar Physics* **10**(1), 5 (2013) <https://doi.org/10.12942/lrsp-2013-5>